Environmental Science & Technology

pubs.acs.org/est

Article

Surface-Phosphorylated Ceria for Chlorine-Tolerance Catalysis

Yuetan Su, Kexin Cao, Yunhao Lu, Qingjie Meng, Qiguang Dai, Xueqing Luo, Hanfeng Lu, Zhongbiao Wu, and Xiaole Weng*

Cite This: *Environ. Sci. Technol.* 2024, 58, 1369−1377

Read Online

ACCESS | Metrics & More | Article Recommendations | Supporting Information

ABSTRACT: An improved fundamental understanding of active site structures can unlock opportunities for catalysis from conceptual design to industrial practice. Herein, we present the computational discovery and experimental demonstration of a highly active surface-phosphorylated ceria catalyst that exhibits robust chlorine tolerance for catalysis. Ab initio molecular dynamics (AIMD) calculations and *in situ* near-ambient pressure X-ray photoelectron spectroscopy (*in situ* NAP-XPS) identified a predominantly HPO_4 active structure on $CeO_2(110)$ and $CeO_2(111)$ facets at room temperature. Importantly, further elevating the temperature led to a unique hydrogen (H) atom hopping between coordinatively unsaturated oxygen and the adjacent P═O group of HPO_4. Such a mobile H on the catalyst surface can effectively quench the chlorine radicals ($Cl^•$) via an orientated reaction analogous to hydrogen atom transfer (HAT), enabling the surface-phosphorylated CeO_2-supported monolithic catalyst to exhibit both expected activity and stability for over 68 days during a pilot test, catalyzing the destruction of a complex chlorinated volatile organic compound industrial off-gas.

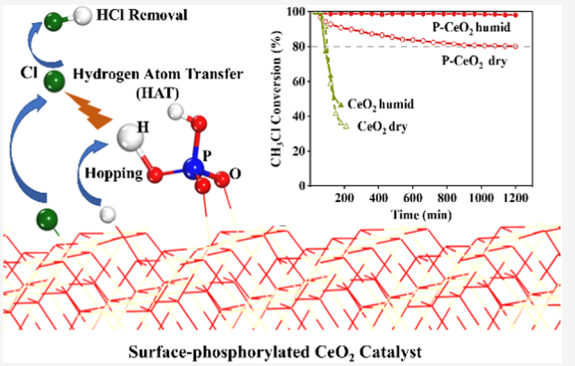

KEYWORDS: *CeO_2, surface phosphorylation, chlorine tolerance, chlorinated organics, environmental catalysis*

1. INTRODUCTION

Chlorine radicals ($Cl^•$) have been identified as a powerful reagent for the efficient functionalization of $C(sp^3)$−H bonds under mild conditions.[1] This radical-mediated strategy benefits a wide range of industrially important reactions, including alkylation, alkenylation, arylation, acylation, and amination.[2−5] However, reactive $Cl^•$ often causes undesirable consequences in environmental reactions. For instance, atmospheric chlorine-initiated reactions can lead to the formation of tropospheric ozone and fine particulate matter ($PM_{2.5}$). Estimations suggest that daily maximum 1 h of O_3 and averaged $PM_{2.5}$ levels in the Yangtze River Delta region of China can be enhanced by up to 4 and 2−6%, respectively.[6] Likewise, the risk of hazardous polychlorinated side products induced by chlorine radicals remains a significant challenge in environmental catalysis, especially during the catalytic destruction of chlorinated organics. These organics are important pollutants emitted primarily from chlorine chemical industries, including pharmaceuticals, agrochemicals, and plastics.[7,8]

The $C(sp^3)$−Cl bonds in chlorinated organics are with lower dissociation free energy than $C(sp^3)$−H bonds, and when cleaved on metal/metal oxide catalysts, they typically form metal−chlorine bonds (M^n−Cl, where M represents high-valent metals). This phenomenon can hinder active site regeneration and lead to severe catalyst deactivation.[9] For decades, significant efforts have been dedicated to solving the issue of chlorine poisoning on industrially viable catalysts. Various strategies based on the concept of "efficient Cl desorption" have been employed, including high-temperature operations that induce a semi-Deacon reaction to form Cl_2.[10−12] However, the high-temperature approach tends to induce the formation of chlorine radicals ($Cl^•$), as evidenced by the electron paramagnetic resonance (EPR) probe.[13] These radicals then participate in generating unavoidable polychlorinated side products, including dioxins.[7] As a result, finding effective ways to quench these chlorine radicals ($Cl^•$) in the catalytic destruction of chlorinated organics becomes crucial to reduce the environmental risk of hazardous polychlorinated side products and potential dioxin formation. This stands in stark contrast to the aforementioned chlorine radical-mediated $C(sp^3)$−H bond functionalization.

Quenching $Cl^•$ typically requires an adduct that can preferentially provide electrons over the $C(sp^3)$−H bond functionalization to fill the outermost electron shell of the Cl atom. However, due to their high reactivity, selectively quenching $Cl^•$ remains a great challenge in environmental catalysis. Hydrogen atom transfer (HAT) is a chemical transformation consisting of the concerted movement of two

Received: August 24, 2023
Revised: October 17, 2023
Accepted: November 21, 2023
Published: December 4, 2023

https://doi.org/10.1021/acs.est.3c06878
Environ. Sci. Technol. 2024, 58, 1369−1377

elementary particles—a proton and an electron—between two substrates in a single kinetic step.[14] H atom insertion can be accomplished through hydrogen spillovers and the codoping of electrons and protons.[15,16] Recently, the authors proposed an analogous HAT approach to quench Cl• by creating a specific hydrolysis site on metal oxide catalysts. At this site, H_2O can be preferentially activated and might provide H atoms to efficiently remove Cl• as HCl at mild temperatures (≤400 °C) instead of Cl_2 (which is formed via the combination of two Cl•).[17−19] The resulting surface-phosphorylated CeO_2 catalysts demonstrated robust destruction of chlorinated organics, including dichloromethane (CH_2Cl_2) and chlorobenzene, without the formation of polychlorinated congeners, even under industrially relevant conditions. Other subsequent works, such as surface phosphorylation on WO_x, γ-Al_2O_3, and Co_3O_4, have also shown similar performance in such reactions.[20−23] However, to date, the precise phosphate active structures on CeO_2 and the exact mechanisms involved in selectively quenching Cl• remain unclear. This lack of clarity is primarily attributed to the absence of sensitive techniques for quantitatively determining and *in situ* tracking of the light hydrogen atoms in phosphate during the reactions.

In this study, we employed *in situ* near-ambient pressure X-ray photoelectron spectroscopy (*in situ* NAP-XPS) and ab initio molecular dynamics (AIMD) to establish atomic description of the precise phosphate structures on the CeO_2 surface, along with density functional theory (DFT) calculations and experimental studies to unravel the mechanisms involved in quenching Cl• on different facet-exposed CeO_2. Our findings demonstrate that phosphates mainly exist as a HPO_4 structure on the predominated CeO_2(110) and CeO_2(111) surfaces. Importantly, we discovered that H on the CeO_2 surface displays a unique H atom hopping feature from the surface (Ce−O) to phosphate (P−O). The H can hop between the adjacent coordinatively unsaturated oxygen of CeO_2 and P═O of phosphates at elevated temperatures. This mobile H hopping remarkably facilitates the formation of HCl, via an oriented reaction analogous to hydrogen atom transfer (HAT), ensuring robust catalytic destruction of chloromethane on rod-shaped CeO_2 catalysts. Subsequently, we subjected a surface-phosphorylated CeO_2-supported monolithic catalyst to a pilot test. The catalyst achieved robust destruction of a complex chlorinated organic industrial off-gas for over 68 days. Our work paves the way for the discovery of a wide range of robust and efficient heterogeneous catalysts for chlorine-tolerance catalysis and highlights that the improved fundamental understanding of active site structures can unlock opportunities for catalysis, from conceptual design to industrial practice.

2. MATERIALS AND METHODS

2.1. Computational Method. All of the first-principles spin-polarized calculations were performed by using the Vienna Ab initio Simulation Package[24−26] (VASP5.4.4) with the Perdew−Burke−Ernzerhof functional.[27] The cutoff energy with a projector-augmented wave (PAW) method[28,29] was set at 400 eV. DFT + *U* was used in this study to properly describe the 4f states in cerium with the value of 5 eV, which tends to be inaccurately represented in standard DFT.[30] In molecular dynamics simulation, ab initio molecular dynamics (AIMD) was employed to evaluate the geometric construction of phosphate species, and canonical ensemble (NVT) conditions were imposed by the Nose−Hoover thermostat with a target temperature of 350 °C. The MD step was set to 0.5 fs, and the initial 2 ps (4000 steps) data were discarded during the equilibration period (see details in the Supporting Information, SI).

2.2. Catalyst Preparation. For the synthesis of the CeO_2 rod (hereafter referred to as CeO_2), a total of 1.736 g of $Ce(NO)_3{\cdot}6H_2O$ and 19.2 g of NaOH were first dissolved in 10 and 70 mL of deionized water, respectively. Then, the two solutions were mixed and continuously stirred for 30 min. The mixed solution was then transferred to a Teflon-lined stainless-steel autoclave and hydrothermally treated at 100 °C for 24 h. After hydrothermal treatment in the preparation, the formed solids were recovered by centrifugation and washed with deionized water and ethanol several times, followed by drying at 80 °C for 12 h.

CeO_2 and phosphate-functionalized CeO_2 (denoted as P-CeO_2) in the shape of rods were synthesized based on previous works.[18] P-CeO_2 was prepared by using an incipient-wetness impregnation method. A total of 4 g of CeO_2 and 100 mL of H_3PO_4 (1 mol/L) solution were mixed at room temperature and stirred for 1 h. The mixture solution was then washed with deionized water several times until the pH approached about 7, followed by drying at 80 °C for 12 h.

12 g of the surface-phosphorylated CeO_2-supported catalyst powder and 0.3 g of binder were mixed with 6 g of 30% silica sol and 30 mL of deionized water. The mixture was stirred for 30 min, and the pH of the liquid was adjusted to 5 using a 1 mol/L nitric acid solution. After continuous stirring for 8 h, a coating slurry was formed. The cordierite honeycomb ceramic was immersed in the slurry for 30 s and then removed. Compressed air was used to blow through the cordierite honeycomb channels, and the sample was subsequently left to dry naturally. Afterward, the sample was placed in an oven and dried at 80 °C for 4 h, then transferred to a muffle furnace, and calcined at 400 °C for 2 h with a heating rate of 10 °C/min.

2.3. Catalyst Characterization and Catalytic Activity Measurements. The details of TMP−^{31}P NMR, ^{31}P CP MAS spectra and ^{1}H−^{31}P HETCOR spectra, in situ near-ambient pressure X-ray photoelectron spectroscopy (in situ NAP-XPS), chloromethane temperature-programmed surface reaction (CH_3Cl-TPSR) measurements, off-gas quantitative measurements, and ion chromatograph instrument measurements are shown in the Supporting Information, SI. The catalytic activity was measured in a continuous fixed-bed quartz tubular reactor with a thermocouple placed at the center to ensure an accurate temperature, which was reported in our previous research. The details of the industrial pilot experiment and dioxin measurements are also shown in the Supporting Information, SI.

3. RESULTS AND DISCUSSION

3.1. Quantitative Identification of CeO_2 Exposure Facets. Rod-shaped CeO_2 has been demonstrated to exhibit the best performance in the catalytic destruction of chlorinated organics compared to octahedron-shaped and cubic-shaped ones.[31] Therefore, rod-shaped CeO_2 was selected as the investigated catalyst for the subsequent structural analysis and modeling. Detailed experiments on the syntheses and characterizations of rod-shaped CeO_2 and its surface phosphorylation (denoted as P-CeO_2) are described above. Our previous characterizations[18] have shown that the P loading on the CeO_2 rod at ca. 6.64 g/kg catalyst (0.6 wt %) corresponds to 1.18 P atoms/nm^2 and such a low P loading

https://doi.org/10.1021/acs.est.3c06878
Environ. Sci. Technol. 2024, 58, 1369−1377

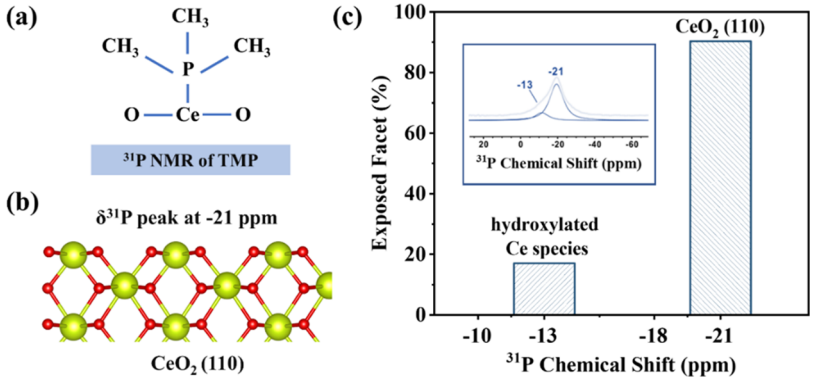

Figure 1. Schematic illustration of the (a) TMP−^{31}P NMR spectrum and (b) facet-dependent Ce species on top CeO_2 surfaces. (c) Qualitative and quantitative results from the deconvoluted TMP−^{31}P NMR Spectra of CeO_2 rods.

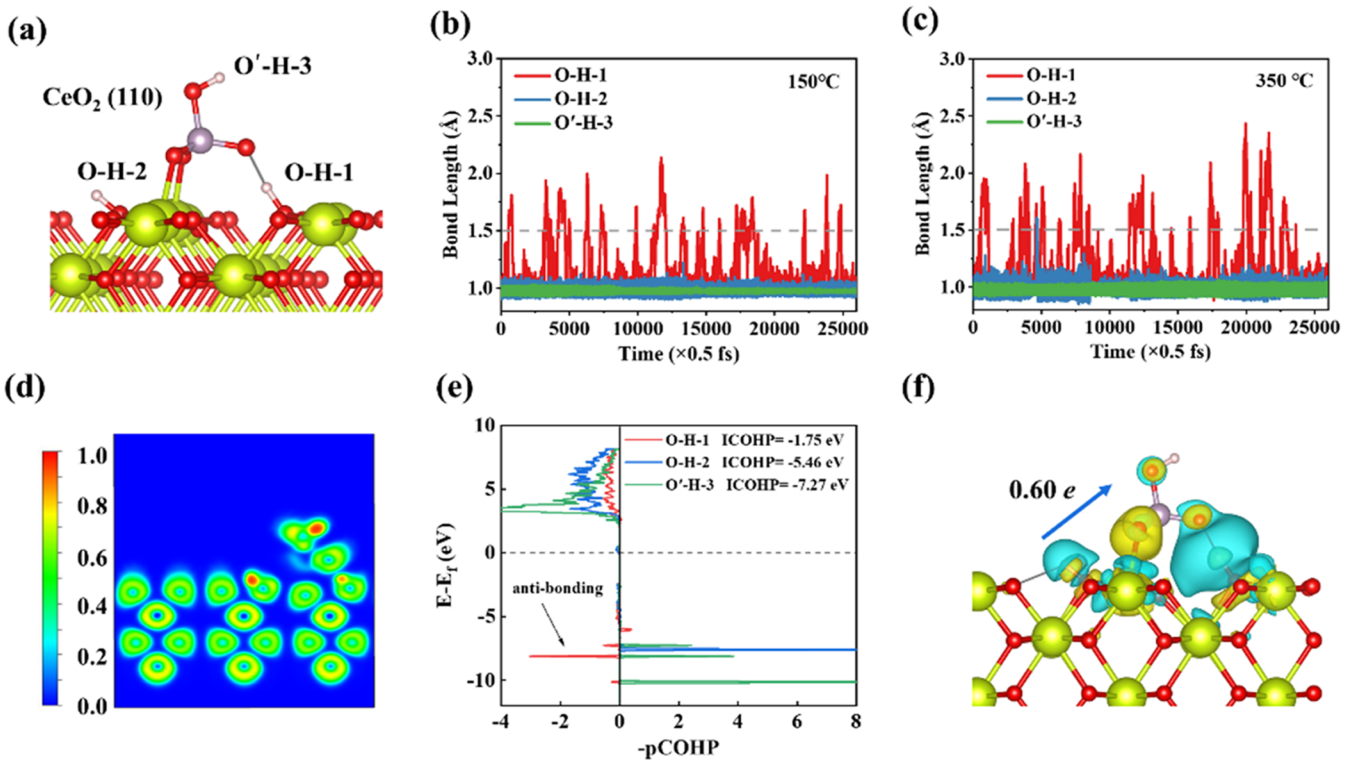

Figure 2. (a) Schematic structure model of H_3PO_4 on the CeO_2(110) surface. Olivine, red, purple, and white balls represent Ce, O, P, and H atoms, respectively. (b) Bond lengths of three O−H bonds on CeO_2(110) at 150 °C and (c) 350 °C. (d) Electron localization function (ELF) of H_3PO_4 on the CeO_2(110) surface. (e) −pCOHP of three O−H bonds of H_3PO_4 on the CeO_2(110) surface. The positive and negative values represent bonding and antibonding character, respectively. (f) Corresponding charge density difference of H_3PO_4 on the CeO_2(110) surface. The yellow and cyan isosurfaces stand for the charge accumulation and depletion regions, respectively.

does not alter the crystallinity, surface area, and morphology of CeO_2.

As the terminal facets of CeO_2 can significantly impact the adsorption and activation of reactants,[32−34] we utilized the trimethylphosphine (TMP)−^{31}P nuclear magnetic resonance (NMR) probe to establish the fingerprint of rod-shaped CeO_2 facets for subsequent structural modeling. The TMP molecule can act as a Lewis base probe and tends to adsorb on coordinatively unsaturated metal cations, resulting in variations in the signals of ^{31}P chemical shifts (δ^{31}P) in ^{31}P NMR. Metal cations (e.g., Ce^{4+} and Ce^{3+}) with different acid strengths on their respective facets can thereby be discriminated by the varied δ^{31}P of TMP-cation complex, while a strong Lewis acid site interacts with TMP in a stronger chemical bond, thus shifting the δ^{31}P to positive ppm.[35,36] Herein, only CeO_2 rods were subjected to the TMP−^{31}P NMR probe as phosphate can competitively adsorb the TMP and interfere with the discrimination of exposed facets.

Figure 1 illustrates the TMP−^{31}P NMR probe of CeO_2 rods, showing two peaks at ca. = −13 and −21 ppm. According to the facet assignments by Tan et al. in ref 36, the δ^{31}P peak at −13 ppm corresponds to hydroxylated CeO_2(111) species, while the peak at −21 ppm is assigned to the (110) facet. In contrast, a benchmark octahedron-shaped CeO_2 exhibited an intense peak at −18 ppm corresponding to the predominated (111) facet and a small peak at −10 ppm for hydroxylated CeO_2(111) species (see Figure S1a,b). The δ^{31}P peak shifts between the (110) and (111) facets are related to their Lewis

https://doi.org/10.1021/acs.est.3c06878
Environ. Sci. Technol. 2024, 58, 1369−1377

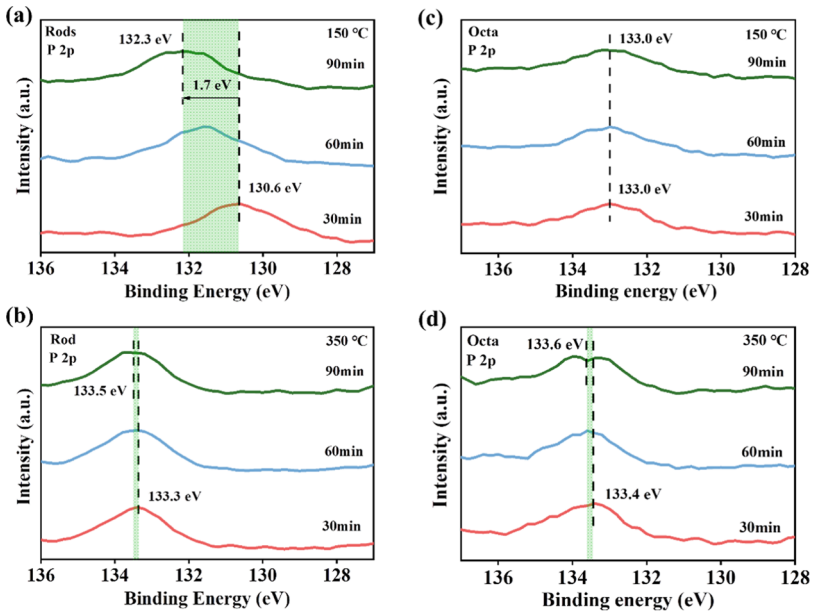

Figure 3. *In situ* NAP-XPS P 2p spectra of P-CeO_2 (a, b) rods and (c, d) octahedrons at 150 and 350 °C.

acidities, where the latter, having a low electron density at the Ce site, exhibits a higher Lewis acidity than the former, thereby shifting the δ^{31}P to positive ppm. Quantification of each δ^{31}P peak area indicated that the (110) facets in CeO_2 rods accounted for 82.9% of the total facet exposure, making them the main exposed facet, which is consistent with previous findings.[36]

3.2. Solid-State NMR Probe of CeO_2 Rods and P-CeO_2. To identify the precise surface P speciation on phosphorylated CeO_2 rods, solid-state nuclear magnetic resonance (ssNMR) with ^{31}P magic angle spinning (CP MAS) was conducted. In Figure S2b, the ^{31}P CP MAS spectrum showed a distinct δ^{31}P peak at −5.27 ppm, flanked by a pair of spinning sidebands on phosphorylated CeO_2 rods. Typically, orthophosphate species (see Figure S2a) resonate between −5 and 10 ppm, while pyrophosphates are a few ppm upfield from this range.[37,38] Therefore, orthophosphate is the most likely configuration of phosphates on the P-CeO_2. Moreover, no bulk $CePO_4$ phase was detected in ssNMR, as its two characteristic δ peaks (−55 ppm for rhabdophane and −90 ppm for monazite[39]) were absent. Furthermore, a two-dimensional (2D) ^{31}P/^{1}H dipolar heteronuclear correlation (HETCOR) (see Figure S2c) was conducted to probe the interaction of the P and H nuclei. The HETCOR spectrum indicated that the ^{31}P sites correlating with two types of protons, where the ^{1}H projection exhibited a resonance at ca. 8.0 ppm attributing to P−OH groups, as the chemical shift of P−OH falls between 7.0 and 16.8 ppm, and the other resonance at ca. 5.5 ppm, can be attributed to the H weakly bound to CeO_2.[38] However, due to the lack of H nuclei sensitivity, ssNMR cannot differentiate between the H_2PO_4, HPO_4, and PO_4 structures on the P-CeO_2 surface.

3.3. Surface P Speciation Analyzation. Ab initio molecular dynamics (AIMD) calculations were then employed to distinguish the surface P speciation on (P-CeO_2). Considering the preferential exposure of (110) facets in the CeO_2 rods, a (110) terminal model was constructed for subsequent AIMD calculations using a theoretical lattice constant of 5.447 Å (see Figure S3). The initial structure for AIMD simulations was optimized to a local minimum. Initial structural optimization showed that after the H_3PO_4 molecule adsorbed on the surface of CeO_2 (see Figure 2a), two H atoms would dissociate to O on the surface (Ce−O, displayed as O), while the other was still in the phosphate group (P−O, displayed as O′). Variations of temperature and energy against time for the AIMD calculation indicated that models have reached balanced states (Figure S5). As shown in Figure 2b,c and Movie S1 (350 °C), an interesting finding is that the H atom in one of the three O−H bonds (denoted as O−H-1) exhibited unusually high mobility. This H atom, adjoining coordinatively unsaturated oxygen on the CeO_2(110) surface, tended to attack adjacent P ═ O bonds on phosphates and quickly returned to the CeO_2(110) surface. The O−H-1 bond length ranged from 0.9 to 2.3 Å at 350 °C, comparatively longer than the other two O−H bonds (0.9−1.2 Å), confirming the greater unstableness of the H atom in O−H-1. Further projected density of states (PDOS, see Figure S6) and Bader charge calculations also demonstrated that after surface phosphorylation, CeO_2 transferred ca. 0.60*e* electrons to phosphates (see Figure 2f). This leads to a reduced charge density of the O−H-1 bond, accompanied by an unstable H atom within the bond. Such a decreased electron occupation in both the O and Ce atoms (neighboring to phosphates) has been verified by their shifts to higher binding energy (BE) in respective O 1s and Ce 3d XPS spectra, as reported in our previous work.[18] Notably, a similar unstable H movement with a relatively lower frequency was also observed at 150 °C (Figure 2b).

Crystal orbital Hamiltonian population (COHP) analyses were further performed to quantitatively assess the strength of the three O−H bonds on the P-CeO_2(110) surface. Figure 2e illustrates that the most mobile O−H-1 exhibited abundant antibonding states in the region of −5 to −10 below the Fermi level. In contrast, O−H-2 and O′−H-3 showed the most bonding states in these regions, indicating a stronger bonding feature in their respective O−H bonds. The stronger bonding features of O−H-2 and O′−H-3 were further confirmed by their corresponding integrated COHP (ICOHP) values, which were found to be −7.27 and −5.46 eV, respectively, much

https://doi.org/10.1021/acs.est.3c06878
Environ. Sci. Technol. 2024, 58, 1369−1377

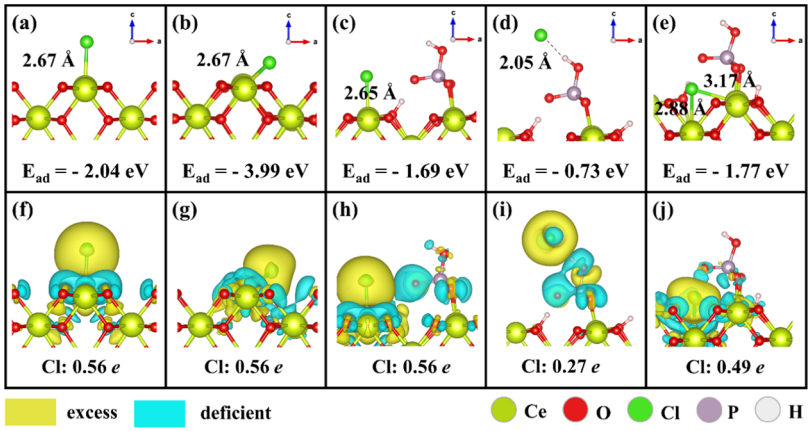

Figure 4. Optimized geometry structures and adsorption energies of Cl on (a) $CeO_2(110)$, (b) O_v-$CeO_2(110)$, (c) Ce−P−$CeO_2(110)$, (d) H−P−$CeO_2(110)$, and (e) O_v-P-$CeO_2(110)$, with corresponding differential charge density (f−j). The yellow and cyan isosurfaces stand for the charge accumulation and depletion regions, respectively. Olivine, red, green, purple, and white balls represent Ce, O, Cl, P, and H atoms, respectively.

stronger than that of O−H-1 (at −1.75 eV). Additionally, the COHP analysis of the O−H bond on the $CeO_2(110)$ surface (see Figure S7) also displayed a significantly more negative ICOHP (at −4.23 eV), validating the stronger antibonding feature observed in the O−H-1 bonds on P-$CeO_2(110)$. For the benchmark P-$CeO_2(111)$, AIMD calculations and electron localization function calculations were also performed. As shown in Figure S8c,d and Movie S2 (350 °C), the H in the O−H-1 bond on P-$CeO_2(111)$ also exhibited a hopping feature at elevated temperature, but with much less mobility compared to P-$CeO_2(110)$. Phosphate exhibits distinct adsorption behaviors on various surfaces, leading to diverse charge transfer phenomena. In the case of P-$CeO_2(111)$, Bader charge calculations reveal that CeO_2 transferred 0.83 *e* electrons to phosphates (see Figure S8a), indicating a higher electron transfer compared to the $CeO_2(110)$ surface. On the (110) surface, a greater number of electrons are required to maintain the phosphorus state compared to the (111) surface, primarily due to the reduced electron transfer from the surface to the phosphoric, aligning with the higher mobility of H atoms on the P-$CeO_2(110)$ surface. Furthermore, the corresponding integrated COHP (ICOHP) values (see Figure S8e) for the three O−H bonds on the P- $CeO_2(111)$ surface (−4.80, −5.16, and −6.78 eV) were much stronger than that of the O−H-1 bond (−1.75 eV) on the P-$CeO_2(110)$ surface. This observation is further supported by electron localization function (ELF) calculations (see Figures 2d and S8b), which indicate that the typical H atoms on the P-$CeO_2(111)$ surface are more stable compared to those of O−H-1 on the (110) surface.

The high mobility of H atoms on P-$CeO_2(110)$ was further demonstrated by using *in situ* near-ambient pressure X-ray photoelectron spectroscopy (*in situ* NAP-XPS). As shown in Figure 3, the *in situ* P 2p XPS spectrum of (110)-exposed P-CeO_2 exhibited a consistent shift toward higher binding energy (BE) at 150 °C and remained stable at 350 °C. This indicates that the P−O bond underwent surface reconstruction during the heat treatments. The constant shift was attributed to dynamic mobile H desorption (likely forming H_2O with −OH on CeO_2), resulting in a decreased electron cloud density around the P atoms. In contrast, P-CeO_2 exposed to the (111) facet did not exhibit any shift at 150 °C over time, indicating a strong localization of its H atoms, which aligns with the AIMD calculations. Based on the AIMD calculations and *in situ* NAP-XPS results, we concluded that surface phosphorylation on the $CeO_2(110)$ surface enables an ultrahigh H atom mobility between P═O and coordinatively unsaturated oxygen neighboring phosphates. This enhanced mobility might facilitate the quenching of $Cl^•$ and suppress the formation of highly toxic polychlorinated side products during the catalytic destruction of chlorinated organics.[18]

3.4. Chlorine Adsorption and H_2O Activation Behaviors. Chlorine adsorption behaviors on $CeO_2(110)$ and P-CeO_2 were further investigated by using density functional theory (DFT) calculations. The oxygen vacancy sites of P-CeO_2 were considered and are shown in Figure S4 and Table S1. The adsorption energy of Cl, denoted as E_{ad}(Cl), is calculated on three sites of $CeO_2(110)$ and P-$CeO_2(110)$ (see Figure 4): (1) Lewis acid site (Ce atom), (2) Brønsted acid site (P−OH), and (3) oxygen vacancy site. For $CeO_2(110)$, the E_{ad}(Cl) on oxygen vacancy (−3.99 eV) is more negative than that on the stoichiometric Ce site (−2.04 eV) (see Figure 4a,b), indicating that dissociated Cl atoms preferentially bond to vacancies on $CeO_2(110)$, which is consistent with previous studies.[40] While for P-$CeO_2(110)$, the E_{ad}(Cl) at the Lewis acid site, Brønsted acid site, and oxygen vacancy decreased to −1.69, −0.73, and −1.77 eV, respectively (see Figure 4c−e). Notably, the presence of phosphate groups weakens the surface bonding of Cl, and the preferentially dissociated Cl at the vacancy site tends to diffuse and bond to nearby Ce atoms due to their similar E_{ad}(Cl) (−1.77 vs −1.69 eV). The DFT results suggest that the stronger affinity of Cl on $CeO_2(110)$, with a more negative E_{ad}(Cl) value, particularly at vacancies, could potentially exacerbate the chlorine poisoning of CeO_2 due to the hindered oxygen activation and subsequent C−Cl dissociation.[40,41] In contrast, the weakened interaction between Cl and the P-$CeO_2(110)$ surface indicates the easier removal for Cl from surface-phosphorylated $CeO_2(110)$. Moreover, the facilitated Cl diffusion at vacancies would promote the regeneration of oxygen vacancies for O_2 activation and could potentially be captured by H−O sites via hydrogen bonds, resulting in the release of HCl.[42] Further differential charge density calculations and Bader charge analysis (see Figure 4f−j) confirmed that the substituted Cl at the vacancy site or the adsorbed Cl atop the Ce atom accepts 0.56*e* from the $CeO_2(110)$ surface and that from the P-CeO_2 is 0.49*e* and 0.27*e* at the vacancy site and phosphate site, respectively,

https://doi.org/10.1021/acs.est.3c06878
Environ. Sci. Technol. 2024, 58, 1369−1377

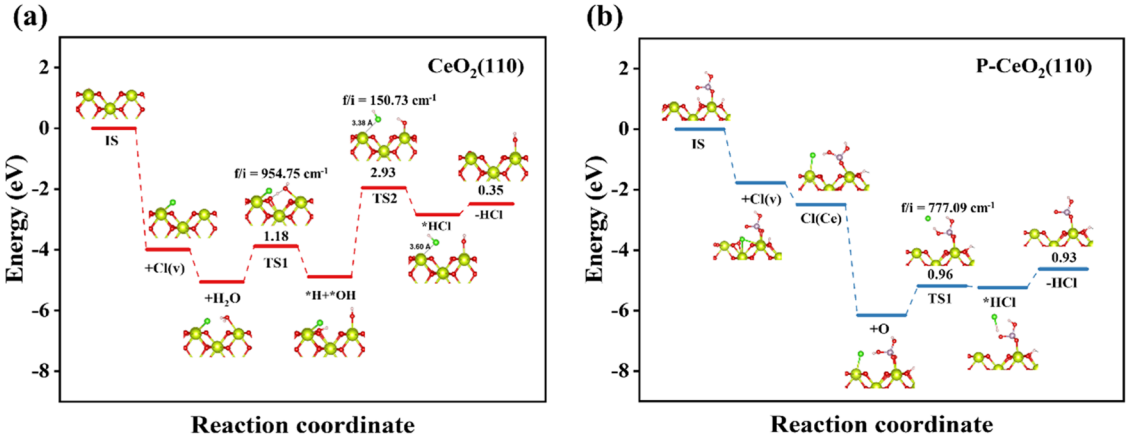

Figure 5. Reaction energy profiles and related structures of dechlorination on (a) $CeO_2(110)$ and (b) P-$CeO_2(110)$. Olivine, red, purple, green, and white balls represent Ce, P, Cl, and H atoms, respectively.

confirming that the interaction of Cl from its occupied sites on $CeO_2(110)$ was decreased after surface phosphorylation.

Water vapor activation can facilitate the surface regeneration of chlorinated oxide catalysts by providing and replenishing H protons for Cl desorption.[42] Herein, we calculated the adsorption energy of H_2O, denoted as $E_{ad}(H_2O)$, on the three sites of $CeO_2(110)$ and P-$CeO_2(110)$ (see Figure S9a,b). We found that H_2O molecules tend to adsorb molecularly on stoichiometric Ce atoms with an $E_{ad}(H_2O)$ of −0.96 eV, while they directly dissociate on oxygen vacancy sites with an $E_{ad}(H_2O)$ of −1.89 eV for $CeO_2(110)$. The dissociated OH from H_2O molecules has a bond length slightly shorter than the original one (0.98 vs 0.99 Å), suggesting that oxygen vacancies are the primary active sites for H_2O dissociating on $CeO_2(110)$. However, Cl is shown to preferentially adsorb on the oxygen vacancy owing to a relatively negative E_{ad} (Cl) compared to E_{ad} (H_2O). Consequently, most oxygen vacancy sites will be blocked by adsorbed Cl and become inaccessible for H_2O activation as well as oxygen activation, leading to an inevitable deactivation of $CeO_2(110)$. For P-$CeO_2(110)$, the E_{ad} (H_2O) values at the Lewis acid site, Brønsted acid site, and oxygen vacancy are −1.19, −0.22, and −0.80 eV, respectively (see Figure S9c−e). In contrast to the direct dissociation of H_2O on the oxygen vacancies of $CeO_2(110)$, H_2O adsorbs molecularly on all three sites of P-$CeO_2(110)$, with preferential adsorption on Lewis acid sites. This leads to the elongation of the OH bond length from 0.99 to 1.03 Å, and the H in the elongated OH bond is expected to replenish the mobile H atom for P-$CeO_2(110)$.

3.5. HCl Formation Pathways Proposed by DFT Calculations. Detailed chlorine desorption energy barriers from $CeO_2(110)$ and P-$CeO_2(110)$ were calculated to elucidate the mechanism of HCl formation and surface regeneration in the presence of H_2O and excessive oxygen. Previously, we have demonstrated that the desorption of Cl from the CeO_2-supported surface at high temperatures can generate highly reactive chlorine radicals ($Cl^•$).[13] These $Cl^•$ are expected to either form HCl by reacting with H or form Cl_2 through their combination (i.e., Deacon reaction). Generally, the former is preferred as the $Cl^•$ can be quickly quenched to suppress the formation of polychlorinated side products.

As shown in Figure 5, the first step for $CeO_2(110)$ is Cl adsorption on the vacancy site with an adsorption energy E_{ad} (Cl) of −3.99 eV. Subsequently, direct dissociation of H_2O occurs near the vacancy site, along with the dissociated OH group bonding to a surface Ce atom and the dissociated H atom bonding to a surface O. The energy barrier for H_2O dissociation is 1.18 eV, and the reaction energy is 0.17 eV. Then, the H atom reacts with a dissociated Cl atom to form HCl with an energy barrier of 2.93 eV. The desorption of HCl is the final step, with a desorption energy of 0.35 eV. The unoccupied oxygen vacancy can be restored by O_2 activation. The rate-determining step of Cl removal on $CeO_2(110)$ is the formation of HCl, with the corresponding energy barrier of 2.93 eV.

For P-$CeO_2(110)$, the first step involves Cl adsorption on the vacancy site with E_{ad}(Cl) of −1.77 eV. However, the adsorbed Cl at the vacancy site tends to migrate to adjacent Lewis acid sites owing to their similar E_{ad} (Cl) under the action of hopping H, and H will migrate from the surface to the phosphate. Then, the oxygen vacancy is readily restored by excessive O_2. Subsequently, the Ce−Cl bond cleaves, releasing the $Cl^•$ from the $CeO_2(110)$ surface, along with an electron transfer from Cl to the neighboring Ce (IV) atom. These $Cl^•$ are then attacked by the mobile and active H atoms originating from H_2PO_4 phosphate to form HCl with the corresponding energy barrier of 0.96 eV.

The DFT results suggested that the presence of mobile H atoms efficiently quenches the $Cl^•$ via an orientated reaction analogous to hydrogen atom transfer (HAT), which can suppress the formation of polychlorinated side products, even dioxins. The desorption of HCl is the final step, with a desorption energy of 0.93 eV. The rate-determining step of Cl desorption on P-$CeO_2(110)$ is also the formation of HCl, with the corresponding energy barrier being 0.96 eV, which is much lower than that for $CeO_2(110)$ (2.93 eV). Notably, the consumed H atoms in P-$CeO_2(110)$ can be easily and continuously replenished by H_2O dissociation at the Ce site next to the phosphate group, with an energy barrier for H_2O dissociation as low as 0.27 eV and a reaction energy of 0.08 eV (see Figure S10). This ensures the existence of sufficient mobile H atoms on P-$CeO_2(110)$ for HCl generation. Notably, similar reaction pathways are observed in the benchmark $CeO_2(111)$ and P-$CeO_2(111)$, as illustrated in Figure S11. Surface phosphorylation facilitates the formation of HCl as the rate-determining step, reducing the corresponding energy barrier from 3.96 to 1.30 eV.

https://doi.org/10.1021/acs.est.3c06878
Environ. Sci. Technol. 2024, 58, 1369−1377

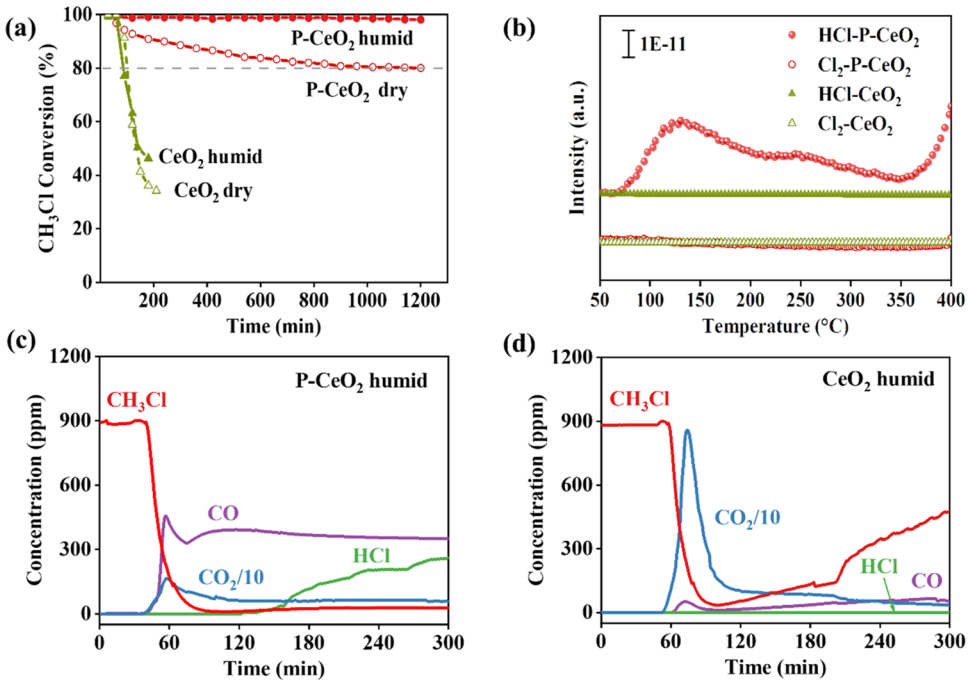

Figure 6. (a) Stability of CeO_2 and P-CeO_2 with and without water vapor at 350 °C. (b) TPSR results of HCl and Cl_2 on CeO_2 and P-CeO_2 from 50 to 400 °C without water. (c) Real-time concentration changes of each component were monitored by the Gasmat spectrometer of CeO_2 and (d) P-CeO_2 under humid conditions. Reaction conditions in the above experiment: GHSV = 10,000 mL/h, 900 ppm of CH_3Cl, 10% O_2, 2% H_2O (when used), 350 °C.

3.6. Experimental Confirmation in Efficient HCl Desorption. To confirm the role of phosphate in facilitating HCl formation on the P-CeO_2 surface, we conducted the catalytic destruction of CH_3Cl (with a large C−Cl bond dissociation free energy of 339 kcal/mol) as a model reaction on both CeO_2 rods and P-CeO_2. Figure 6a shows that P-CeO_2 achieved a steadier CH_3Cl conversion over 80% for at least 1200 min at 350 °C (the temperature of complete conversion in light-off curves) under dry conditions, exhibiting much greater stability compared to that of pristine CeO_2 rods, which experienced deactivation after 80 min. The presence of water vapor (2 vol %) further assisted in maintaining a steady conversion without decline. The enhanced stability of P-CeO_2 is attributed to the accelerated chlorine removal in the form of HCl, as confirmed by the temperature-programmed surface reaction (TPSR) profiles shown in Figure 6b. On P-CeO_2, the mass spectrometry (MS) intensities of HCl predominated over Cl_2, while on CeO_2, both species remained at baselines at the temperature ≤400 °C. Quantitatively, as depicted in Figure S12, the amount of produced chlorine species in the off-gas (enriched in a 0.02 mol/L NaOH solution at 350 °C for 2 h) on P-CeO_2 under humid conditions was over 70 times higher than that on CeO_2. Additionally, online quantification of the off-gas using a Gasmat infrared spectrometer (see Figure 6c,d) also confirmed that the generation of HCl on the P-CeO_2 was much higher than that on CeO_2 during the reaction course, and there were no polychlorinated alkanes (e.g., dichloromethane and trichloromethane) having been detected in their off-gas, suggesting the preferential reaction of the H atom with $Cl^•$ over the C(sp^3)−H bond functionalization. These results provide direct evidence that surface phosphorylation on CeO_2 efficiently induces Cl desorption in the form of HCl during the catalytic destruction of chlorinated organics, consistent with AIMD and DFT calculations.

In summary, we conducted a comprehensive study combining computational and experimental approaches to identify a novel surface-phosphorylated CeO_2 catalyst capable of efficiently destructing chlorinated organics from industrial exhausts. Initially, AIMD calculations and an in situ XPS probe revealed the unique H hopping feature of surface-phosphorylated CeO_2 rods. Subsequent DFT calculations and catalyst testing confirmed that phosphorylation reduced Cl adsorption on the CeO_2(110) surface, and the hopping H atoms between P═O of phosphates and adjacent coordinatively unsaturated oxygen of CeO_2(110) quenched the chlorine radical ($Cl^•$) through an orientated reaction analogous to hydrogen atom transfer (HAT). Remarkably, an industrial pilot test of a commercially available CeO_2-supported monolithic catalyst based on the surface phosphorylation strategy (see Figure S13a,b) demonstrated robust performance for 68 days in the catalytic destruction of a complex chlorinated organic exhaust gas (see Figure S13c,d) and resulted in a total off-gas dioxin concentration of only 15.98 pg I-TEQ/Nm^3 (see Figure S14 and Table S2), well below both the European Union (EU) emission limit and the Chinese national emission standard limit of 0.1 ng I-TEQ/Nm^3. Further characterizations indicated that there were no significant alterations in the height of XRD diffraction peaks (see Figure S15), and there were unconspicuous changes in the elemental composition (see Table S3) of the monolithic catalyst before and after the pilot reaction. We anticipate that surface phosphorylation will constantly lead to the discovery of a wide range of robust and efficient catalysts for chlorine-tolerance catalysis, which is crucial for sustainable industrial processes.

https://doi.org/10.1021/acs.est.3c06878
Environ. Sci. Technol. 2024, 58, 1369−1377

■ ASSOCIATED CONTENT

Supporting Information

The Supporting Information is available free of charge at https://pubs.acs.org/doi/10.1021/acs.est.3c06878.

Computational method, catalyst characterization, and catalytic activity measurements (PDF)

Movie S1: AIMD trajectories showing H_3PO_4 on CeO_2(110) surface at 350 °C (MP4)

Movie S2: AIMD trajectories showing H_3PO_4 on CeO_2(111) surface at 350 °C (MP4)

■ AUTHOR INFORMATION

Corresponding Author

Xiaole Weng − *Key Laboratory of Environment Remediation and Ecological Health, Ministry of Education, College of Environmental and Resource Sciences, Zhejiang University, Hangzhou 310058, P. R. China; ZJU-Hangzhou Global Scientific and Technological Innovation Center, Hangzhou 311200, P. R. China;* orcid.org/0000-0003-2997-571X; Email: xlweng@zju.edu.cn

Authors

Yuetan Su − *Key Laboratory of Environment Remediation and Ecological Health, Ministry of Education, College of Environmental and Resource Sciences, Zhejiang University, Hangzhou 310058, P. R. China*

Kexin Cao − *Key Laboratory of Environment Remediation and Ecological Health, Ministry of Education, College of Environmental and Resource Sciences, Zhejiang University, Hangzhou 310058, P. R. China*

Yunhao Lu − *Key Laboratory of Silicon Materials, School of Materials Science and Engineering, Zhejiang University, Hangzhou 310027, P. R. China;* orcid.org/0000-0001-6825-7206

Qingjie Meng − *School of Civil & Environmental Engineering and Geography Science, Ningbo University, Ningbo 315211, P. R. China*

Qiguang Dai − *Key Laboratory for Advanced Materials, Research Institute of Industrial Catalysis, School of Chemistry and Molecular Engineering, East China University of Science and Technology, Shanghai 200237, P. R. China;* orcid.org/0000-0001-6764-6744

Xueqing Luo − *ZJU-Hangzhou Global Scientific and Technological Innovation Center, Hangzhou 311200, P. R. China*

Hanfeng Lu − *Institute of Catalytic Reaction Engineering, College of Chemical Engineering, Zhejiang University of Technology, Hangzhou 310014, P. R. China*

Zhongbiao Wu − *Key Laboratory of Environment Remediation and Ecological Health, Ministry of Education, College of Environmental and Resource Sciences, Zhejiang University, Hangzhou 310058, P. R. China; Zhejiang Provincial Engineering Research Centre of Industrial Boiler & Furnace Flue Gas Pollution Control, Hangzhou 310058, P. R. China;* orcid.org/0000-0003-0182-5971

Complete contact information is available at: https://pubs.acs.org/10.1021/acs.est.3c06878

Author Contributions

All authors contributed to the development of the manuscript. All authors have approved the final version of the manuscript. X.W. conceived and led the study. Y.S. performed catalytic activity experiments, DFT calculations, and data analyses and wrote the first draft of the manuscript. K.C. provided TMP−^{31}P NMR data. Y.L. provided thought and guidance of calculations. Q.M. polished the manuscript. Q.D. provided support of catalyst synthesis. X.L. performed the industrial pilot test. H.L. and Z.W. discussed the results and commented on the manuscript.

Notes

The authors declare no competing financial interest.

■ ACKNOWLEDGMENTS

The authors acknowledge the financial support provided by the National Key R&D Program of China (No. 2022YFC3701603), the National Natural Science Foundation of China (Nos. 22176169 and 52070168), the Key R&D Plan of Zhejiang Province (No. 2023C03127), and the Fundamental Research Funds for the Central Universities (No. 226-2022-00150). The authors acknowledge the in situ near-ambient pressure X-ray photoelectron spectroscopy (in situ NAP-XPS) support provided by Bin Zhou from State Key Joint Laboratory of Environment Simulation and Pollution Control, School of Environment, Tsinghua University, Beijing, China. The authors acknowledge the NMR support provided by Hua-Dong Xue from Department of Chemistry, Zhejiang University, Hangzhou, China.

■ REFERENCES

(1) Gonzalez, M. I.; Gygi, D.; Qin, Y. Z.; Zhu, Q. L.; Johnson, E. J.; Chen, Y. S.; Nocera, D. G. Taming the Chlorine Radical: Enforcing Steric Control over Chlorine-Radical-Mediated C-H Activation. *J. Am. Chem. Soc.* **2022**, *144* (3), 1464−1472.

(2) Shields, B. J.; Doyle, A. G. Direct C(sp^3)-H Cross Coupling Enabled by Catalytic Generation of Chlorine Radicals. *J. Am. Chem. Soc.* **2016**, *138* (39), 12719−12722.

(3) Deng, H. P.; Fan, X. Z.; Chen, Z. H.; Xu, Q. H.; Wu, J. Photoinduced Nickel-Catalyzed Chemo- and Regioselective Hydroalkylation of Internal Alkynes with Ether and Amide alpha-Hetero C(sp^3)-H Bonds. *J. Am. Chem. Soc.* **2017**, *139* (38), 13579−13584.

(4) Deng, H. P.; Zhou, Q.; Wu, J. Microtubing-Reactor-Assisted Aliphatic C-H Functionalization with HCl as a Hydrogen-Atom-Transfer Catalyst Precursor in Conjunction with an Organic Photoredox Catalyst. *Angew. Chem., Int. Ed.* **2018**, *57* (39), 12661−12665.

(5) Yang, Q. M.; Wang, Y. H.; Qiao, Y. S.; Gau, M.; Carroll, P. J.; Walsh, P. J.; Schelter, E. J. Photocatalytic C-H activation and the subtle role of chlorine radical complexation in reactivity. *Science* **2021**, *372* (6544), 847−852.

(6) Li, J. Y.; Zhang, N.; Wang, P.; Choi, M.; Ying, Q.; Guo, S.; Lu, K. D.; Qiu, X. H.; Wang, S. X.; Hu, M.; Zhang, Y. H.; Hu, J. L. Impacts of chlorine chemistry and anthropogenic emissions on secondary pollutants in the Yangtze river delta region. *Environ. Pollut.* **2021**, *287*, No. 117624.

(7) He, C.; Cheng, J.; Zhang, X.; Douthwaite, M.; Pattisson, S.; Hao, Z. P. Recent Advances in the Catalytic Oxidation of Volatile Organic Compounds: A Review Based on Pollutant Sorts and Sources. *Chem. Rev.* **2019**, *119* (7), 4471−4568.

(8) Li, T.; Li, H.; Li, C. L. A review and perspective of recent research in biological treatment applied in removal of chlorinated volatile organic compounds from waste air. *Chemosphere* **2020**, *250*, No. 126338.

(9) Lin, F. W.; Xiang, L.; Zhang, Z. M.; Li, N.; Yan, B. B.; He, C.; Hao, Z. P.; Chen, G. Y. Comprehensive review on catalytic degradation of Cl-VOCs under the practical application conditions. *Crit. Rev. Environ. Sci. Technol.* **2022**, *52* (3), 311−355.

(10) Zhang, N. N.; Guo, Y. L.; Guo, Y.; Dai, Q. G.; Wang, L.; Dai, S.; Zhan, W. C. Synchronously constructing the optimal redox-acidity

of sulfate and RuO_x Co-modified CeO_2 for catalytic combustion of chlorinated VOCs. *Chem. Eng. J.* **2023**, *454*, No. 140391.
(11) Dai, Q. G.; Bai, S. X.; Wang, J. W.; Li, M.; Wang, X. Y.; Lu, G. Z. The effect of TiO_2 doping on catalytic performances of Ru/CeO_2 catalysts during catalytic combustion of chlorobenzene. *Appl. Catal., B* **2013**, *142*−*143*, 222−233.
(12) Zhang, X.; Dai, L. Y.; Liu, Y. X.; Deng, J. G.; Jing, L.; Yu, X. H.; Han, Z.; Zhang, K. F.; Dai, H. X. 3DOM CeO_2-supported Ru_yM (M = Au, Pd, Pt) alloy nanoparticles with improved catalytic activity and chlorine-tolerance in trichloroethylene oxidation. *Catal. Sci. Technol.* **2020**, *10* (11), 3755−3770.
(13) Shen, K.; Gao, B.; Xia, H. Q.; Deng, W.; Yan, J. R.; Guo, X. H.; Guo, Y. L.; Wang, X. Y.; Zhan, W. C.; Dai, Q. G. Oxy-Anionic Doping: A New Strategy for Improving Selectivity of Ru/CeO_2 with Synergetic Versatility and Thermal Stability for Catalytic Oxidation of Chlorinated Volatile Organic Compounds. *Environ. Sci. Technol.* **2022**, *56* (12), 8854−8863.
(14) Mader, E. A.; Davidson, E. R.; Mayer, J. M. Large ground-state entropy changes for hydrogen atom transfer reactions of iron complexes. *J. Am. Chem. Soc.* **2007**, *129* (16), 5153−5166.
(15) Prins, R. Hydrogen Spillover. Facts and Fiction. *Chem. Rev.* **2012**, *112* (5), 2714−2738.
(16) Xie, L. Y.; Zhu, Q.; Zhang, G. Z.; Ye, K.; Zou, C. W.; Prezhdo, O. V.; Wang, Z. W.; Luo, Y.; Jiang, J. Tunable Hydrogen Doping of Metal Oxide Semiconductors with Acid-Metal Treatment at Ambient Conditions. *J. Am. Chem. Soc.* **2020**, *142* (9), 4136−4140.
(17) Dai, Q. G.; Zhang, Z. Y.; Yan, J. R.; Wu, J. Y.; Johnson, G.; Sun, W.; Wang, X. Y.; Zhang, S.; Zhan, W. C. Phosphate-Functionalized CeO_2 Nanosheets for Efficient Catalytic Oxidation of Dichloromethane. *Environ. Sci. Technol.* **2018**, *52* (22), 13430−13437.
(18) Dai, X. X.; Wang, X. W.; Long, Y. P.; Pattisson, S.; Lu, Y. H.; Morgan, D. J.; Taylor, S. H.; Carter, J. H.; Hutchings, G. J.; Wu, Z. B.; Weng, X. L. Efficient Elimination of Chlorinated Organics on a Phosphoric Acid Modified CeO_2 Catalyst: A Hydrolytic Destruction Route. *Environ. Sci. Technol.* **2019**, *53* (21), 12697−12705.
(19) Weng, X. L.; Meng, Q. J.; Liu, J. J.; Jiang, W. Y.; Pattisson, S.; Wu, Z. B. Catalytic Oxidation of Chlorinated Organics over Lanthanide Perovskites: Effects of Phosphoric Acid Etching and Water Vapor on Chlorine Desorption Behavior. *Environ. Sci. Technol.* **2019**, *53* (2), 884−893.
(20) Zhang, L.; Deng, W.; Cai, Y. P.; Dai, Q. G.; Guo, L. M. Comparative Studies of Phosphate-Modified CeO_2 and Al_2O_3 for Mechanistic Understanding of Dichloromethane Oxidation and Chloromethane Formation. *ACS Catal.* **2020**, *10* (21), 13109−13124.
(21) Yu, X. H.; Dai, L. Y.; Peng, Y.; Deng, J. G.; Liu, Y. X.; Jing, L.; Zhang, X.; Hou, Z. Q.; Wang, J.; Dai, H. X. High Selectivity to HCl for the Catalytic Removal of 1,2-Dichloroethane Over RuP/3DOM WO_x: Insights into the Effects of P-Doping and H_2O Introduction. *Environ. Sci. Technol.* **2021**, *55* (21), 14906−14916.
(22) Xu, S.; Ma, Y. K.; Zhang, K. F.; Jia, A. P.; Chen, J.; Luo, M. F.; Wang, Y.; Lu, J. Q. Catalytic oxidation of dichloromethane over phosphate-modified Co_3O_4: Improved performance and control of byproduct selectivity by Co_3O_4 defects and surface acidity. *Appl. Surf. Sci.* **2022**, *606*, No. 154924.
(23) Liu, H.; Yang, J.; Jia, Y. Y.; Wang, Z. Q.; Jiang, M. X.; Shen, K.; Zhao, H. L.; Guo, Y. L.; Guo, Y.; Wang, L.; Dai, S.; Zhan, W. C. Significant Improvement of Catalytic Performance for Chlorinated Volatile Organic Compound Oxidation over RuO_x Supported on Acid-Etched Co_3O_4. *Environ. Sci. Technol.* **2021**, *55* (15), 10734−10743.
(24) Kresse, G.; Hafner, J. Ab initio molecular dynamics for open-shell transition metals. *Phys. Rev. B: Condens. Matter* **1993**, *48* (17), 13115−13118.
(25) Kresse, G. Ab-Initio Molecular-Dynamics for Liquid-Metals. *J. Non-Cryst. Solids* **1995**, *192*−*193*, 222−229.
(26) Kresse, G.; Furthmuller, J. Efficiency of ab-initio total energy calculations for metals and semiconductors using a plane-wave basis set. *Comput. Mater. Sci.* **1996**, *6* (1), 15−50.
(27) Perdew, J. P.; Burke, K.; Ernzerhof, M. Generalized Gradient Approximation Made Simple. *Phys. Rev. Lett.* **1996**, *77* (18), 3865−3868.
(28) Blöchl, P. E. Projector augmented-wave method. *Phys. Rev. B: Condens. Matter* **1994**, *50* (24), 17953−17979.
(29) Blochl, P. E. The Projector-Augmented Wave (PAW) Method and Dynamical Properties of Organometallic Compounds. In *Abstracts of Papers of the American Chemical Society*; American Chemical Society, 1995; Vol. *209*.
(30) Liu, J. C.; Wang, Y. G.; Li, J. Toward Rational Design of Oxide-Supported Single-Atom Catalysts: Atomic Dispersion of Gold on Ceria. *J. Am. Chem. Soc.* **2017**, *139* (17), 6190−6199.
(31) Huang, H.; Dai, Q. G.; Wang, X. Y. Morphology effect of Ru/CeO_2 catalysts for the catalytic combustion of chlorobenzene. *Appl. Catal., B* **2014**, *158*−*159*, 96−105.
(32) Paier, J.; Penschke, C.; Sauer, J. Oxygen Defects and Surface Chemistry of Ceria: Quantum Chemical Studies Compared to Experiment. *Chem. Rev.* **2013**, *113* (6), 3949−3985.
(33) Divins, N. J.; Angurell, I.; Escudero, C.; Perez-Dieste, V.; Llorca, J. Influence of the support on surface rearrangements of bimetallic nanoparticles in real catalysts. *Science* **2014**, *346* (6209), 620−623.
(34) Montini, T.; Melchionna, M.; Monai, M.; Fornasiero, P. Fundamentals and Catalytic Applications of CeO_2-Based Materials. *Chem. Rev.* **2016**, *116* (10), 5987−6041.
(35) Zheng, A. M.; Liu, S. B.; Deng, F. P^{31} NMR Chemical Shifts of Phosphorus Probes as Reliable and Practical Acidity Scales for Solid and Liquid Catalysts. *Chem. Rev.* **2017**, *117* (19), 12475−12531.
(36) Tan, Z.; Li, G.; Chou, H.-L.; Li, Y.; Yi, X.; Mahadi, A. H.; Zheng, A.; Edman Tsang, S. C.; Peng, Y.-K. Differentiating Surface Ce Species among CeO_2 Facets by Solid-State NMR for Catalytic Correlation. *ACS Catal.* **2020**, *10* (7), 4003−4011.
(37) Xue, X.; Kanzaki, M. Proton Distributions and Hydrogen Bonding in Crystalline and Glassy Hydrous Silicates and Related Inorganic Materials: Insights from High-Resolution Solid-State Nuclear Magnetic Resonance Spectroscopy. *J. Am. Ceram. Soc.* **2009**, *92* (12), 2803−2830.
(38) Nelson, N. C.; Wang, Z.; Naik, P.; Manzano, J. S.; Pruski, M.; Slowing, I. I. Phosphate modified ceria as a Bronsted acidic/redox multifunctional catalyst. *J. Mater. Chem. A* **2017**, *5* (9), 4455−4466.
(39) Karpowich, L.; Wilcke, S.; Yu, R.; Harley, G.; Reimer, J. A.; De Jonghe, L. C. Synthesis and characterization of mixed-morphology $CePO_4$ nanoparticles. *J. Solid State Chem.* **2007**, *180* (3), 840−846.
(40) Miran, H. A.; Altarawneh, M.; Jiang, Z.-T.; Oskierski, H.; Almatarneh, M.; Dlugogorski, B. Z. Decomposition of selected chlorinated volatile organic compounds by ceria (CeO_2). *Catal. Sci. Technol.* **2017**, *7* (17), 3902−3919.
(41) Yin, L. L.; Lu, G. Z.; Gong, X. Q. A DFT + U study of the catalytic degradation of 1,2-dichloroethane over CeO_2. *Phys. Chem. Chem. Phys.* **2018**, *20* (8), 5856−5864.
(42) Cen, W. L.; Liu, Y.; Wu, Z. B.; Liu, J.; Wang, H. Q.; Weng, X. L. Cl Species Transformation on CeO_2(111) Surface and Its Effects on CVOCs Catalytic Abatement: A First-Principles Investigation. *J. Phys. Chem. C* **2014**, *118* (13), 6758−6766.

https://doi.org/10.1021/acs.est.3c06878
Environ. Sci. Technol. 2024, 58, 1369−1377